Temperature and magnetic field dependent grain boundary structures in skyrmion lattices via a quasiparticle-based mechanism

Kohta Kasai [1,*,†] Chang Liu [1,2,*] Akihiro Uematsu,[1,‡] Tatsuki Kawakane,[1] Tao Xu [1] Yu Wang,[3] Susumu Minami,[1] and Takahiro Shimada [1,§]

[1]*Department of Mechanical Engineering and Science, Kyoto University, Kyoto 615-8540, Japan*
[2]*School of Mechanics and Aerospace Engineering, Southwest Jiaotong University, Chengdu 611756, China*
[3]*Department of Mechanics, School of Civil Engineering, Central South University, Changsha 410083, China*

(Received 28 October 2025; accepted 5 January 2026; published 2 March 2026)

Skyrmion lattices, composed of densely packed ferromagnetic skyrmions, possess unique topological domain structures and can be tuned by external factors like force, magnetic fields, and temperature, making them promising for next-generation spintronic devices. Similar to atomic crystals, lattice defects, such as grain boundaries, exist within skyrmion lattices and are expected to have significant impact on the behaviors of skyrmion lattices. However, even the fundamental structures and external condition dependence of skyrmion grain boundaries remain poorly understood. In this study, we systematically investigated the skyrmion grain boundary structures and their dependence on external fields using phase-field simulations. Our results reveal that skyrmion grain boundaries are stabilized through skyrmion deformation, forming unique quasiparticle-based structures, while they consist of five to seven pair dislocations, analogous to those in conventional crystals. The degree of deformation strongly depends on both temperature and magnetic field: at low temperature and low magnetic field, skyrmions near the grain boundary undergo enhanced deformation, in order to reduce Dzyaloshinskii-Moriya interaction energy. Furthermore, our strain analysis shows that such local skyrmion deformations fundamentally alter the lattice mismatch relaxation mechanisms. These findings not only deepen the fundamental understanding of defect structures in topological magnetic systems but also provide insights relevant to the design of advanced spintronic devices.

DOI: 10.1103/41sh-vktd

I. INTRODUCTION

In recent years, skyrmions have attracted significant research attention due to their remarkable characteristics. Ferromagnetic skyrmions were first observed in chiral magnetic MnSi thin films [1]. Depending on the magnetization distribution, skyrmions can be classified as Néel type or Bloch type [2]. The topological nature contributes to the attractive properties of skyrmions. It provides inherent stability through topological protection and generates unique emergent electromagnetic fields. Such protection also enables particlelike behavior, allowing individual skyrmions to undergo deformation, creation, and annihilation while maintaining distinct identities. For example, the emergent electromagnetic fields enable efficient skyrmion manipulation. Low current densities can achieve high-speed control through topological Hall effects [3] and skyrmion Hall effects [4]. These dynamic properties have prompted proposals for diverse nanodevice applications, including racetrack memory [5], logic devices [6], and synaptic elements for neuromorphic computing [7]. Consequently, skyrmions are recognized as a class of novel topological orders with unique properties and significant technological potential.

In most experimental settings, skyrmions self-assemble into ordered arrays rather than existing as isolated particles, which are known as skyrmion lattices [8]. For ferromagnetic materials, skyrmions lattices are similar to crystalline materials but possess unique quasiparticle properties, which include deformation, creation, and annihilation. Skyrmion lattices may therefore exhibit characteristics significantly different from conventional crystal materials. Research has examined various lattice-specific phenomena, including skyrmion lattice "melting" [9,10], phase transitions between triangular and square configurations [11], and large-scale lattice deformations induced by material strain [12]. In addition, the skyrmion lattices can exhibit defects analogous to conventional crystalline materials. These defects include vacancies [13], dislocations [14–16], and grain boundaries [17–20]. Experimental observations demonstrate that grain boundaries form through aligned dislocation cores, which are analogous to atomic crystals. This formation mechanism resembles particle-based systems and notably influences skyrmion morphology near boundaries [19]. These lattice defects are a fundamental consequence of the quasiparticle nature of skyrmions and are integral to the phase stability of the lattice.

As in conventional crystalline materials, where defects can critically govern macroscopic properties [21], defects in skyrmion lattices are expected to significantly influence their

*These authors contributed equally to this work.
†Contact author: kasai.kohta.72s@st.kyoto-u.ac.jp
‡Contact author: lc@swjtu.edu.cn
§Contact author: shimada.takahiro.8u@kyoto-u.ac.jp

 ©2026 American Physical Society

mechanical and electromagnetic behavior. Grain boundaries can induce other lattice defects [22,23]. Therefore, their presence has a significant impact on the overall properties of the material [24]. For example, the localized disorder near a grain boundary can act as a diffusion pathway for vacancies and is a major cause of segregation, which ultimately leads to crack initiation [25]. Furthermore, from a phenomenological perspective, the energy in the vicinity of a grain boundary is higher than in other regions due to lattice mismatch [26]. Experimental observations have proved that the rotation of crystal orientation in skyrmion lattices can be driven by grain boundaries [18]. Therefore, understanding these effects holds substantial engineering value for the development of skyrmion-based devices. However, despite their fundamental importance, the behavior of skyrmion lattice defects and their impact on lattice properties are not yet well understood. Current research remains limited. Thus, further investigation is still needed to clarify the structure of skyrmion grain boundaries and the control of skyrmion lattices.

In this paper, we investigate the impact of defects on skyrmion lattice structures using the phase-field method. We focus on chiral magnetic MnSi nanothin films as a representative material. Common defects including vacancies, dislocations, and grain boundaries are studied. Specifically, this work elucidates the fundamental characteristics of grain boundary structures, analyzing their dependence on temperature and magnetic fields. Furthermore, the influence of these defects on the surrounding lattice is investigated from both energetic and strain-field perspectives. The findings of this work provide theoretical support for understanding the evolution mechanism and controlling the grain boundaries of ferromagnetic skyrmions. These results also hold significant value for the application of skyrmion lattices in advanced spintronic devices.

The remainder of this paper is organized as follows: Sec. II presents the phase-field modeling of ferromagnetic materials; Sec. III introduces the numerical implications; Sec. IV gives the simulation results and discussions; Sec. VI presents the concluding remarks.

II. THEORETICAL FRAMEWORK

Phase-field modeling for magnetic materials

The total free energy of the magnetic material is expressed as follows [27,28]:

$$F = \int_V (f_{\text{Land}} + f_{\text{exchange}} + f_{\text{DM}} + f_{\text{DMa}} + f_{\text{magnetic}} + f_{\text{elas}})\mathrm{d}V. \tag{1}$$

Here, f_{Land}, f_{exchange}, f_{DM}, f_{DMa}, f_{magnetic}, f_{elas}, and f_{aniso} represent the Landau free energy density, exchange energy density, Dzyaloshinskii-Moriya (DM) interaction energy density, DM interaction anisotropy energy density, energy density due to the magnetic field, elastic energy density, perpendicular magnetic anisotropy energy density, and crystalline magnetic anisotropy energy density, respectively.

The Landau free energy density f_{Land} is given by

$$f_{\text{Land}} = a_0(T - T_c)M^2 + bM^4, \tag{2}$$

in which $M = \sqrt{M_1^2 + M_2^2 + M_3^2}$ represents the mangnitude of the magnetic moment. a_0 and b are the Landau energy coefficients. T and T_c denote the temperature and the Curie temperature, respectively. The Landau free energy density f_{Land} describes the second-order phase transition at T_c. This term ensures that ferromagnetics favors a nonmagnetized state above T_c and a spontaneous magnetization below it, thereby capturing the temperature dependence of the magnetic ordering.

The exchange energy density f_{exchange} arises from quantum mechanical interactions between adjacent spins, which is the function of spatial gradients of the magnetic moment:

$$f_{\text{exchange}} = A\big(M_{1,1}^2 + M_{1,2}^2 + M_{1,3}^2 + M_{2,1}^2 + M_{2,2}^2 + M_{2,3}^2 + M_{3,1}^2 + M_{3,2}^2 + M_{3,3}^2\big), \tag{3}$$

where A is the exchange stiffness coefficient. $M_{i,j}$ represents the partial derivative of M_i with respect to x_j.

The DM interaction energy denstiy f_{DM} is

$$f_{\text{DM}} = D(M_1M_{3,2} - M_1M_{2,3} + M_2M_{1,3} - M_2M_{3,1} + M_3M_{2,1} - M_3M_{1,2}), \tag{4}$$

in which D is the DM interaction constant. The DM interaction acts between neighboring magnetic moments like the exchange interaction. However, it induces a torque between adjacent magnetic moments, which causes the tilting of magnetic moments relative to each other.

Additionally, the DM interaction exhibits anisotropy due to strain inherent in the material. This anisotropy is described by the DM interaction anisotropy energy density f_{DMa}, which can be expressed as follows:

$$f_{\text{DMa}} = f_{\text{DMa1}} + f_{\text{DMa2}} + f_{\text{DMa3}}, \tag{5a}$$

with

$$f_{\text{DMa1}} = \frac{L_{O1}}{M_s^2}[\varepsilon_{11}(M_{1,2}M_3 - M_{1,3}M_2) + \varepsilon_{22}(M_{2,3}M_1 - M_{2,1}M_3) + \varepsilon_{33}(M_{3,1}M_2 - M_{3,2}M_1)], \tag{5b}$$

$$f_{\text{DMa2}} = \frac{L_{O2}}{M_s^2}[\varepsilon_{11}(M_{3,1}M_2 - M_{2,1}M_3) + \varepsilon_{22}(M_{1,2}M_3 - M_{3,2}M_1) + \varepsilon_{33}(M_{2,3}M_1 - M_{1,3}M_2)], \tag{5c}$$

$$f_{\text{DMa3}} = \frac{L_{O3}}{M_s^2}[\varepsilon_{11}M_1(M_{2,3} - M_{3,2}) + \varepsilon_{22}M_2(M_{3,1} - M_{1,3}) + \varepsilon_{33}M_3(M_{1,2} - M_{2,1})], \tag{5d}$$

where L_{Oi} $(i = 1,\ 2,\ 3)$ denote the DM interaction anistropy coefficients.

The magnetic energy density f_{magnetic} is

$$f_{\text{magnetic}} = -\frac{\mu_0}{2}\big(H_1^2 + H_2^2 + H_3^2\big) - \mu_0(H_1M_1 + H_2M_2 + H_3M_3). \tag{6}$$

Here, H_i denotes the magnetic field within the material, and μ_0 is the premeability of vacuum. The magnetic field H_i in Eq. (6) includes contributions from both an externally applied

magnetic field and the internal field generated by the magnetic dipoles. Each magnetic moment can be considered a magnetic dipole, oriented from a positive magnetic charge to a negative one. These dipoles generate a magnetic field that depends on both the arrangement of magnetic moments and the geometry of the structure.

The elastic energy density f_{elas} can be described as

$$\begin{aligned} f_{\text{elas}} = {} & \frac{1}{2}C_{11}\left(\varepsilon_{11}^2+\varepsilon_{22}^2+\varepsilon_{33}^2\right)+2C_{44}\left(\varepsilon_{12}^2+\varepsilon_{23}^2+\varepsilon_{31}^2\right) \\ & +C_{12}(\varepsilon_{11}\varepsilon_{22}+\varepsilon_{22}\varepsilon_{33}+\varepsilon_{33}\varepsilon_{11}) \\ & -\frac{3\lambda_{100}}{2M_s^2}(C_{11}-C_{12})\left(\varepsilon_{11}M_1^2+\varepsilon_{22}M_2^2+\varepsilon_{33}M_3^2\right) \\ & -\frac{6\lambda_{111}}{M_s^2}C_{44}(\varepsilon_{12}M_1M_2+\varepsilon_{23}M_2M_3+\varepsilon_{31}M_3M_1), \end{aligned} \tag{7}$$

in which C_{11}, C_{12}, and C_{44} are the elastic stiffness constants, λ_{100} and λ_{111} are the magnetostriction coefficients, and M_s represents the saturation magnetization. In Eq. (7), the first three terms represent the energy density due to elastic strain, while the last two terms describe the energy density associated with magnetostriction and inverse magnetostriction. Thus, the elastic energy density f_{elas} not only accounts for elastic strain but also reflects the interdependence between magnetic moments and strain.

The spatial and temporal evolution of magnetic moments in the ferromagnetic material is described by the following Landau-Lifshitz-Gilbert (LLG) equation [29]:

$$\frac{\partial M_i}{\partial t} = -\gamma M_i \times H_{\text{eff},i} + \frac{\alpha}{M_s}M_i \times \frac{\partial M_i}{\partial t}, \tag{8}$$

where $H_{\text{eff},i}$ is the effective magnetic field, α is the Gilbert damping constant ($0 \leqslant \alpha \leqslant 1$), and $\gamma = g\frac{\mu_B}{\hbar}$ is the gyromagnetic ratio, with g being the g factor, μ_B the Bohr magneton, and $\hbar$ the reduced Planck constant.

Assuming that the magnetic moments are overdamped, the LLG equation can be reduced to the time-dependent Ginzburg-Landau equation [30,31]:

$$\frac{\partial M_i}{\partial t} = -L\left[\frac{\partial f}{\partial M_i} - \frac{\partial}{\partial x_j}\left(\frac{\partial f}{\partial M_{i,j}}\right)\right], \tag{9}$$

in which $L = \frac{\gamma M_s}{\alpha\mu_0}$ is the kinetic coefficient governing the time evolution of the magnetic moments.

As shown in Eqs. (6) and (7), the behavior of magnetic moments is determined not only by their intrinsic interactions but also by their relationships with the magnetic field and strain. Therefore, the mechanical equilibrium and Maxwell's equation must be satisfied simultaneously:

$$\frac{\partial}{\partial x_j}\left(\frac{\partial f}{\partial \varepsilon_{ij}}\right) = 0, \tag{10}$$

$$\frac{\partial}{\partial x_i}\left(\frac{\partial f}{\partial H_i}\right) = 0. \tag{11}$$

The semi-implicit Fourier-spectral method is used to numerically solve the governing equations Eqs. (9)–(11) [32].

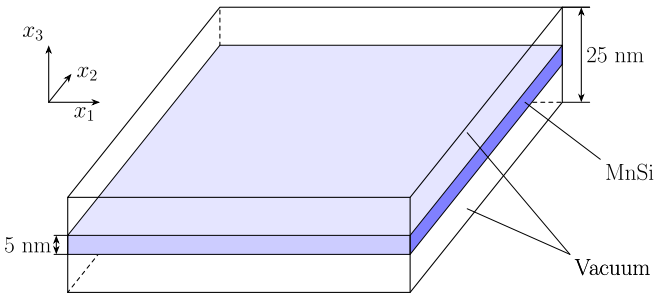

FIG. 1. The schematic illustration of the MnSi thin-film model. The model is periodic along the x_1, x_2, and x_3 directions. The vacuum layers are introduced at the top and bottom of the thin film along the x_3 direction.

III. NUMERICAL IMPLICATION

MnSi is an ideal candidate for the study of skyrmions since it can exhibit a stable skyrmion phase within wide temperature–magnetic field ranges. Therefore, to investigate skyrmion grain boundary structures, the MnSi thin-film model is considered here. Given an MnSi thin film with the thickness of 5 nm, as presented in Fig. 1, periodic boundary conditions are applied along the x_1, x_2, and x_3 directions. To realize the thin-film configuration in the simulation, a 10-nm vacuum layer is introduced at the top and bottom of the thin-film model along the x_3 direction. The material constants for MnSi are listed in Table I. Under appropriate magnetic fields, Bloch-type skyrmions form a triangular lattice in MnSi thin films [8]. Figure 2 illustrates this Bloch-type skyrmion triangular lattice and its unit cell. The dimensions of the unit cell are $\sqrt{3}a$ in the x_1 direction and a in the x_2 direction, where a represents the skyrmion lattice constant. The skyrmion lattice constant a depends on both temperature T and external magnetic field H. To establish the dimensions for our analytical model under various temperature and magnetic field conditions, we first conducted a preliminary simulation to precalculate the equilibrium skyrmion lattice constant $a(T, H)$. Here, the reference

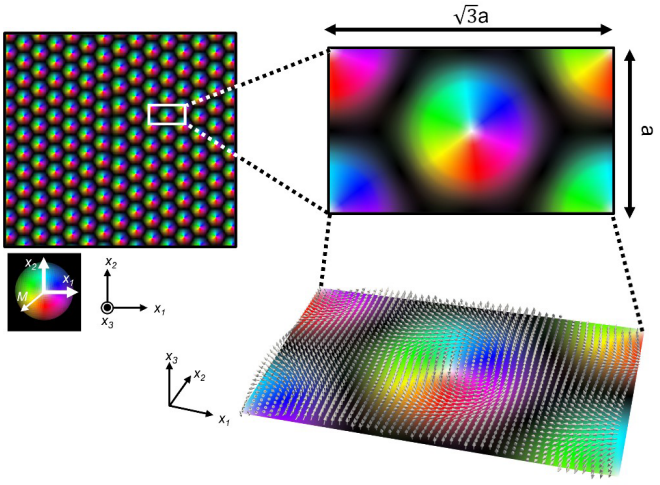

FIG. 2. The triangle lattice and triangle unit cell of the (Bloch-type) skyrmion lattice. The color map indicates the direction of magnetic moments.

TABLE I. Material constants for MnSi. Data are collected from Refs. [27,33].

Landau energy coefficients		Curie temperature	
a_0 [10^{-7} J/(A^2 mK)]	6.44	T_c (K)	29.5
b_0 (10^{-16} J m/A^4)	3.53		
Exchange energy coefficient		DMI constant	
A (10^{-23} J m/A^2)	1.27	D (10^{-14} J/A^2)	1.14
Vacuum permeability		Saturated magnetization	
μ_0 (10^{-7} H/m)	4π	M_s (10^5 A/m)	1.63
Elastic constants		Magnetostrictive coefficients	
C_{11} (GPa)	283	λ_{100} (10^{-6})	3.04
C_{12} (GPa)	64	λ_{111} (10^{-6})	2.26
C_{44} (GPa)	117		

conditions are defined as $T = 22.5$ K, $H = 2 \times 10^5$ A/m, as the skyrmion lattice is known to exhibit relatively stable existence under these parameters. At these reference conditions, the skyrmion lattice constant a is 17.9 nm.

Experimental observations have shown that tilt grain boundaries formed in skyrmion lattices are primarily composed of dislocation core arrays [18–20]. Therefore, the grain boundaries in the skyrmion lattices are constructed by introducing an array of dislocation cores [27], as illustrated in Fig. 3. To maintain the number of skyrmions at the boundaries under periodic boundary conditions, symmetrically opposite grain boundaries are introduced at the center and ends of the thin-film model. This approach follows established methods for simulating grain boundary structures in atomic systems [34]. The misorientation angle for the grain boundary is set to 21.8°. This angle is selected based on its demonstrated stability in the [0001] plane of hexagonal close-packed structures [35,36] and its experimental confirmation in skyrmion lattices [19].

To ensure consistent skyrmion lattice configurations across different temperature and magnetic field conditions, the model dimensions in the x_1 and x_2 directions are precisely determined. This determination is based on two key factors: the geometrical consistency of the grain boundary within a two-dimensional triangular lattice, and the skyrmion lattice constant $a(T, H)$. For example, under the reference conditions ($T = 22.5$ K, $H = 2.0 \times 10^5$ A/m, and $a = 17.9$ nm), the model dimensions are set to $w = 964.8$ nm and

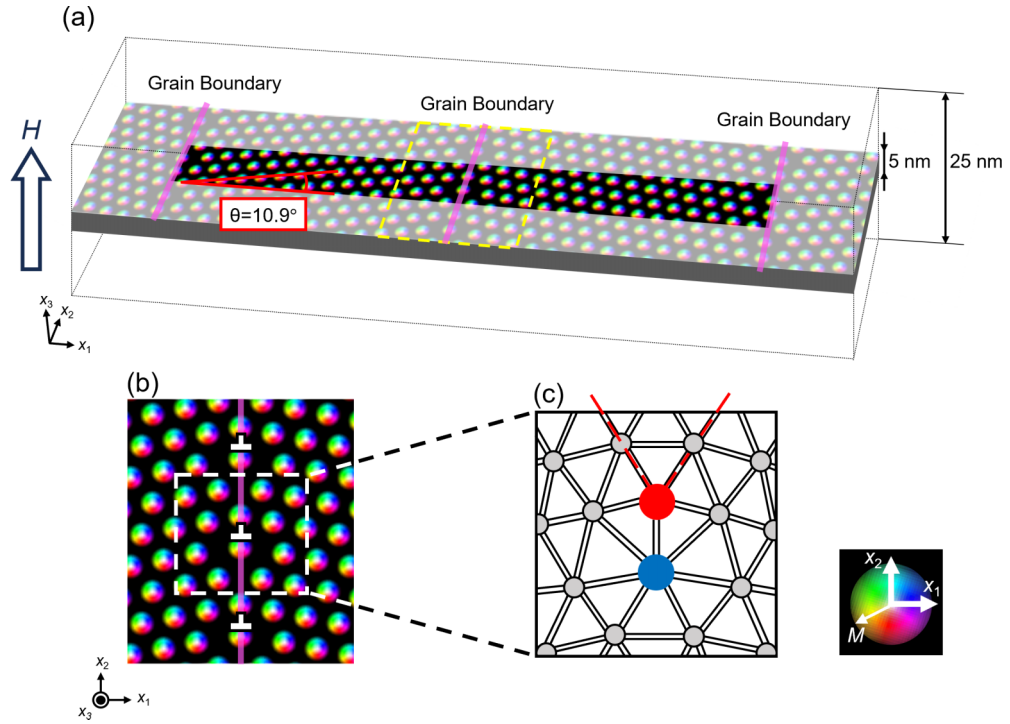

FIG. 3. (a) The schematic illustration of the grain boundary model. The purple line indicates the grain boundary; the arrow and upside-down "T" denote the direction of the applied magnetic field and dislocation core, respectively. (b) The spatial distribution of skyrmions at the grain boundary, corresponding to the magnified region indicated by the yellow dashed rectangle in (a). (c) Core structure of the grain boundary. The blue and red dots show skyrmions surrounded by seven and five skyrmions respectively. The red dashed line demonstrates the excess of the particle line.

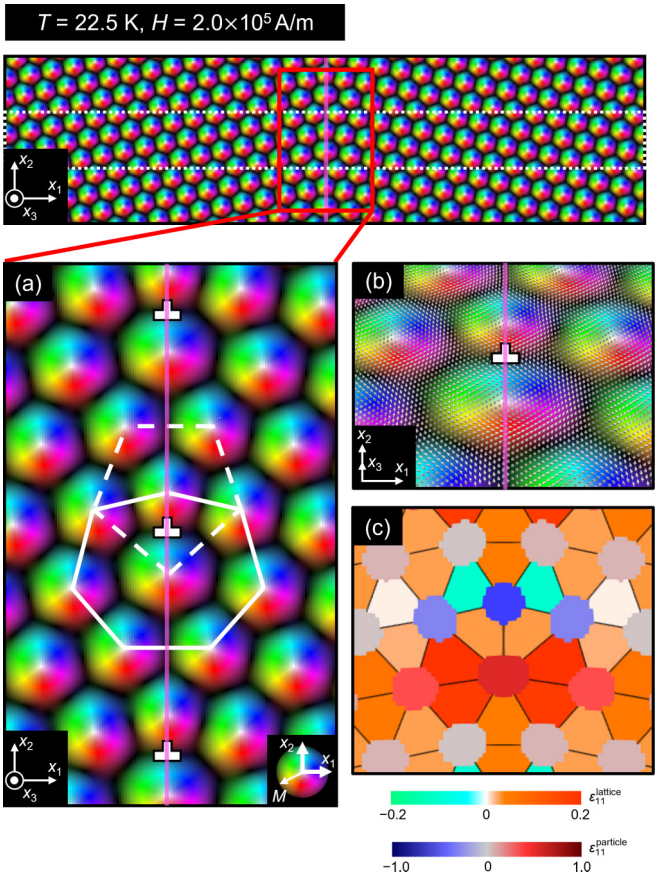

FIG. 4. Configuration of the skyrmion lattice with the grain boundary under reference state $T = 22.5$ K, $H = 2.0 \times 10^5$ A/m. (a) Enlarged area near the grain boundary and (b) the directions of the magnetic moment. The color map indicates the direction of magnetic moments. (c) Strain distribution of the skyrmion lattice and particles.

$h = 830.4$ nm. For the numerical calculations, the model domain is discretized into 539, 50, and 30 elements along the x_1, x_2, and x_3 directions, respectively.

The numerical procedure begins with a preliminary simulation to determine the equilibrium skyrmion lattice constant $a(T, H)$ for each temperature T and magnetic field H. Therefore, by using an appropriate skyrmion lattice constant a for each condition, the influence of the lattice constant can be excluded. The dimensions of the main simulation model are then precisely set based on the precalculated a for each specific condition. For each configuration, the system is relaxed until the change in total free energy between successive time steps (1.0×10^{-2} ns) falls below 10^{-29} J, which defines the thermodynamic equilibrium state.

IV. SIMULATION RESULTS

A. Skyrmion grain boundary structure under the reference condition

The thermodynamically equilibrated grain boundary structure under the reference condition is shown in Figs. 4(a) and 4(b). The grain boundary in equilibrium forms a lattice structure consisting of paired fivefold and sevenfold skyrmions. While skyrmions in a perfect crystal lattice are uniformly sized and circular, significant variations in shape and size for skyrmions are found near the grain boundary.

Edge dislocations in crystalline materials generate spontaneous strain fields. The region below the dislocation core experiences tension, while compressive strain develops above it. Our simulations reveal analogous behavior in skyrmion lattices. Figure 4(c) presents the lattice strain and particle strain distribution in the vicinity of the grain boundary. The lattice strain is defined as an indicator of lattice deformation, with a perfect hexagonal skyrmion lattice serving as the reference [37,38]. In contrast, the particle strain is used to quantify the deformation of individual skyrmions. These strain fields significantly influence skyrmion morphology near dislocation cores. Fivefold skyrmions positioned above the dislocation core undergo compression and exhibit reduced dimensions. Simultaneously, sevenfold skyrmions located below the core respond to tensile strain by elongating along the x_1 direction. This direct correspondence between strain fields and skyrmion morphology demonstrates that skyrmions respond to lattice strain in a manner consistent with their quasiparticle nature, where compression induces contraction and tension causes elongation.

These computational results are also validated by experimental observations. In polycrystalline $FeGe_{1-x}Si_x$ materials, similar deformation patterns at grain boundaries are observed, where fivefold skyrmions shrink while sevenfold skyrmions expand [19]. The remarkable agreement between our simulations and these experimental observations confirms the physical validity of our phase-field approach and the reliability of our findings regarding strain-mediated skyrmion deformation.

Comparing with conventional crystalline material systems, skyrmion lattices exhibit a unique response to lattice strain. Specifically, skyrmions near grain boundaries undergo deformation in response to lattice strain. This strain-responsive behavior highlights the distinctive quasiparticle nature of skyrmions and constitutes a fundamental difference between skyrmion lattices and traditional particle-based systems.

B. Temperature and magnetic field dependence of the skyrmion grain boundary structure

To systematically investigate the influence of temperature and magnetic field, the controlled-variable approach is employed. Additional simulations are performed with varied temperature and magnetic field in this subsection. First, to isolate the effect of temperature, we performed simulations at 18.0, 22.5, and 27.25 K under a constant magnetic field of 2.0×10^5 A/m. Second, to minimize the effect of the magnetic field, we conducted simulations at 1.0×10^5, 2.0×10^5, and 4.0×10^5 A/m at a fixed temperature of 22.5 K.

Figure 5 presents the equilibrium skyrmion lattice structure near the grain boundary at $T = 27.25$ and 18.0 K. At both high and low temperatures, the thermodynamic equilibrium state maintains the dislocation core structure composed of fivefold and sevenfold skyrmions, similar to the reference condition. However, temperature significantly modulates the deformation of skyrmions at the grain boundary. At a high temperature of 27.25 K, skyrmion deformation is largely suppressed, as presented in Fig. 5(a). The skyrmions remain

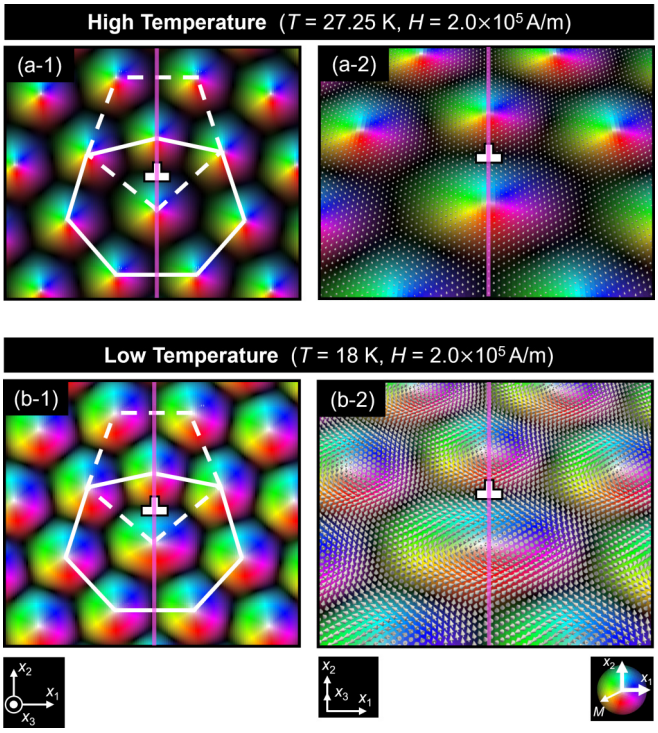

FIG. 5. Skyrmion lattice structures and magnetic moments near the grain boundary under different temperature conditions of (a) $T = 18.0$ K and (b) 27.25 K at a constant magnetic field of $H = 2.0 \times 10^5$ A/m. The size of arrows indicates the magnitude of the magnetic moment.

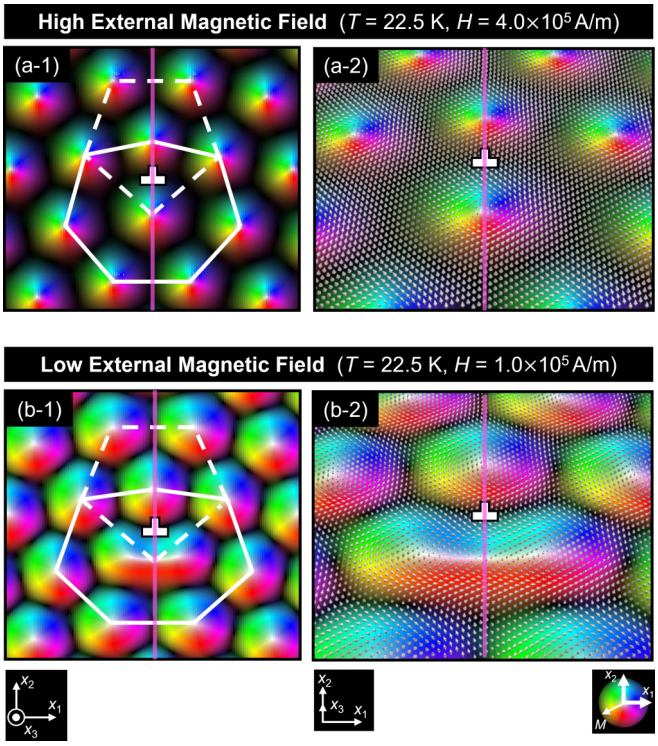

FIG. 6. Skyrmion lattice structures with the grain boundary under different magnetic field conditions of (a) $H = 1.0 \times 10^5$ and (b) 4.0×10^5 A/m at $T = 22.5$ K. The size of arrows indicates the magnitude of magnetic moment.

almost unchanged throughout the lattice, even in the vicinity of the dislocation core.

Conversely, at a low temperature of 18.0 K, the strain-induced deformation becomes more significant, as shown in Fig. 5(b). The sevenfold skyrmions in the tensile region elongate noticeably along the x_1 axis, while the fivefold skyrmions in the compressive region contract. These findings indicate that at high temperatures, skyrmion deformation is suppressed, while at low temperatures, skyrmions near the grain boundary deform in response to the lattice strain field induced by dislocations.

To determine the influence of the magnetic field, we fixed the temperature at $T = 22.5$ K and compared the equilibrium grain boundary structures with the magnitude of magnetic field $H = 1.0 \times 10^5$ and 4.0×10^5 A/m, as shown in Fig. 6. While the fundamental five to seven dislocation core structure is preserved across different field strengths, the morphology of the constituent skyrmions is highly dependent on the field magnitude. Under a high magnetic field ($H = 4.0 \times 10^5$ A/m), skyrmion deformation is suppressed. The skyrmions remain nearly uniform and circular throughout the lattice, showing high rigidity against the local strain field. Conversely, larger deformation of the skyrmions is found under a low magnetic field ($H = 1.0 \times 10^5$ A/m). The sevenfold skyrmions elongate into distinct elliptical shapes along the x_1 axis. This indicates that a lower magnetic field reduces the skyrmions' stability, making them more susceptible to the lattice strain field.

Figure 7 provides a comprehensive comparison of skyrmion deformation under all investigated conditions. Skyrmion deformation is suppressed at higher temperatures and enhanced at lower temperatures. Similarly, higher magnetic fields suppress deformation while lower fields increase it. For all conditions, the skyrmion deformation near the grain boundary consistently corresponds to the local lattice strain field around the dislocation core.

These findings demonstrate that skyrmions exhibit a unique behavior that distinguishes them from conventional crystalline materials. While atomic systems maintain rigid particles regardless of local strain fields, skyrmions actively deform in response to lattice strain. This deformation represents a fundamental quasiparticle characteristic of skyrmion lattices, with the degree of deformation being modulated by temperature and magnetic field conditions.

V. DISCUSSIONS

A. Energy evolution near the grain boundary

Skyrmions near a grain boundary deform in response to local strain, which cannot be observed in conventional crystalline materials. To understand the energetic driving force behind this unique deformation, this section further analyzes the contributions of the different free energy components. Figure 8(a) presents the magnetic moment distribution near the grain boundary. The total free energy drops as the skyrmions deform, as presented in Fig. 8(b).

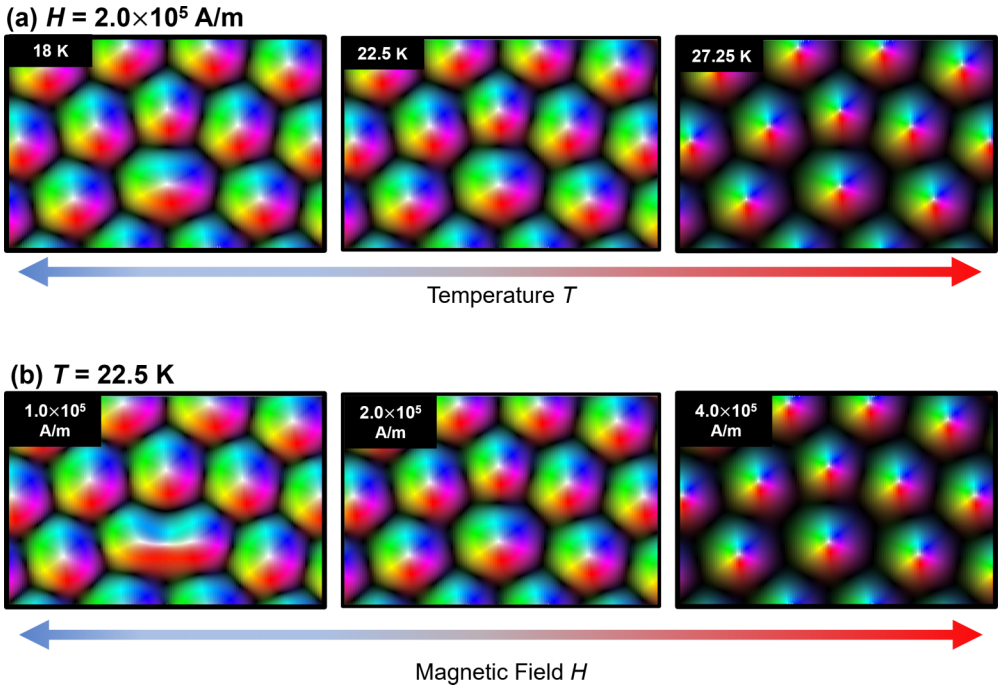

FIG. 7. Dependency of skyrmion lattice structures around the grain boundary on (a) temperature and (b) magnetic field.

The temporal evolution of energy is depicted in Fig. 9. The changes of the anisotropic DM interaction energy density, f_{DMa}, and the elastic energy density, f_{elas}, are negligible. A slight decrease is observed in both f_{Land} and f_{magnetic}. During the evolution, f_{exchange} increases steadily, while f_{DM} gradually decreases.

Then we focus on the vicinity of the grain boundary, and we analyze the skyrmion lattice grain boundary structure under $T = 22.5$ K and $H = 1.0 \times 10^5$ A/m. Figure 10(a) illustrates the temporal evolution of the magnetic moment component M_3 near the grain boundary. Skyrmions far from the grain boundary maintain their original morphology with minimal change. Near the grain boundary, sevenfold skyrmions are gradually elongated into elliptical shapes with the influence of lattice strain. The deformation of the skyrmion lattice is accompanied by a significant evolution in total free energy. Figures 10(b)–10 (e) present the evolution of free energy densities during skyrmion deformation.

The energy calculation reveals the underlying mechanism driving this deformation. For the exchange energy density f_{exchange}, low-energy regions shrink while high-energy regions expand over time, which results in an increase of

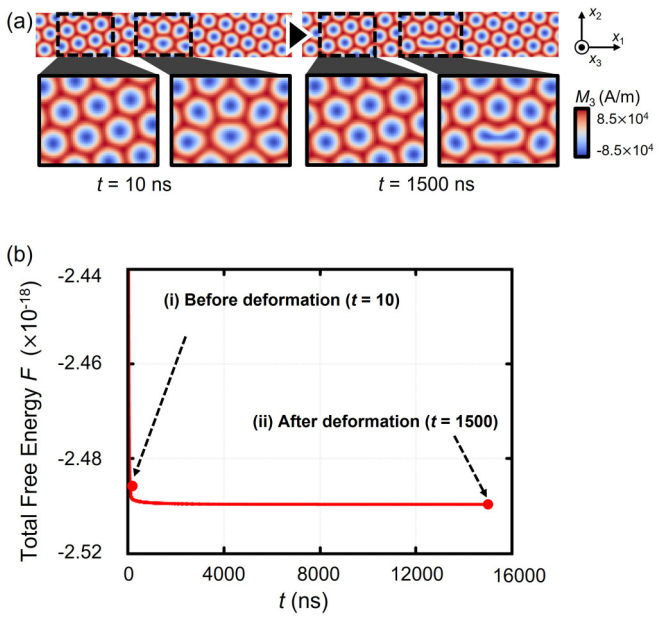

FIG. 8. (a) Enlarged area around the grain boundary on the MnSi model. The color map indicates the component of magnetic moments M_3. (b) The profile of total free energy F with the deformation of skyrmion lattices.

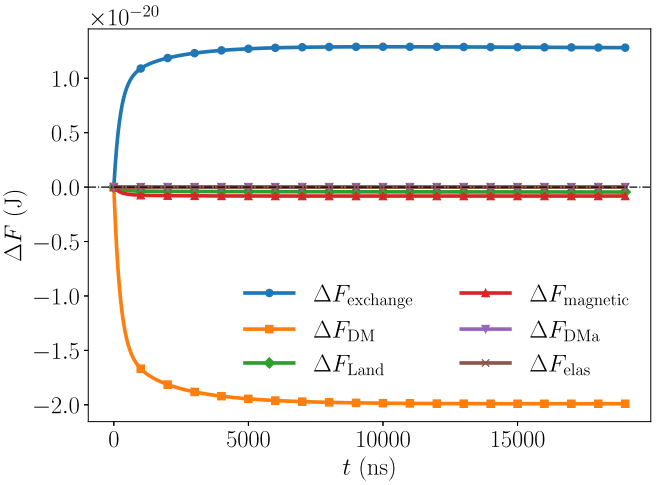

FIG. 9. Temporal evolution of free energy components during skyrmion deformation at $(T, H) = (22.5\ \mathrm{K}, 1.0 \times 10^5\ \mathrm{A/m})$.

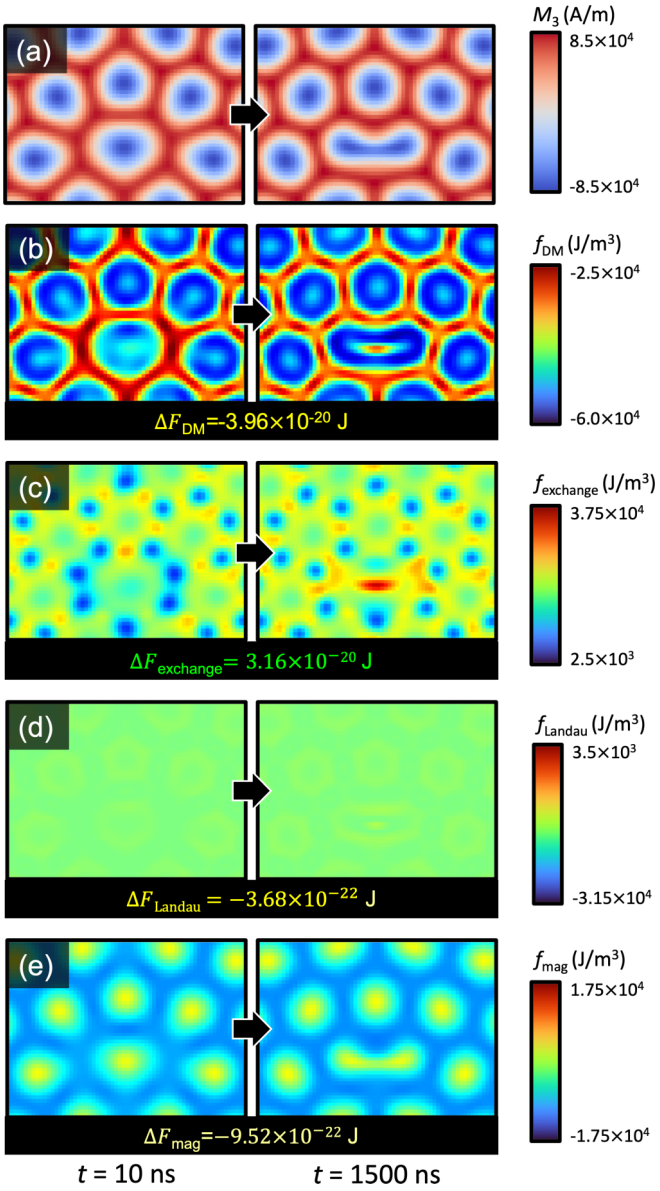

FIG. 10. Temporal evolutions of (a) magnetic moment, (b) f_{DM}, (c) f_{exchange}, (d) f_{Land}, and (e) f_{magnetic} under $T = 22.5$ K and $H = 1.0 \times 10^5$ A/m.

6.24×10^{-5} J/m^2 per unit grain boundary area. Conversely, the DM interaction energy density f_{DM} shows the opposite trend. High-energy regions surrounding sevenfold skyrmions are gradually replaced by low-energy regions, leading to a decrease of 7.83×10^{-5} J/m^2 per unit grain boundary area. The changes in Landau energy f_{Land} and magnetic energy f_{magnetic} are relatively small, indicating that the competition between f_{exchange} and f_{DM} plays the dominant role in driving skyrmion deformation.

This energy competition reflects the fundamental physics of magnetic interactions in skyrmion systems. The exchange interaction favors parallel alignment of magnetic moments, while the DM interaction promotes relative tilting between neighboring moments. These interactions are inherently competitive. The stabilization of f_{DM} drives a larger decrease in the total energy, which outweighs the concurrent increase in f_{exchange}. Consequently, the skyrmion deformation becomes energetically favorable. Furthermore, the energy reduction is most significant in the region near the grain boundary. This indicates that skyrmion deformation stabilizes the grain boundary.

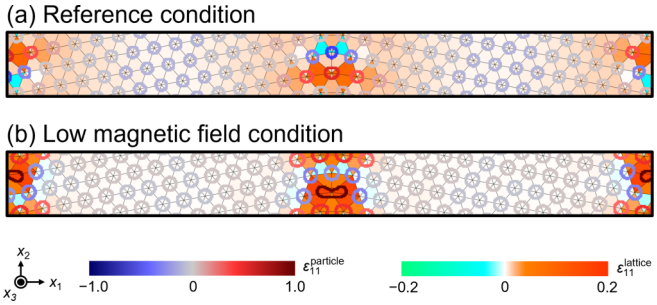

FIG. 11. Lattice strain and particle strain distribution at the (a) reference condition and (b) low magnetic field condition with $H = 1.0 \times 10^5$ A/m.

B. Quasiparticle-based relaxation of the skyrmion grain boundary

Previous sections demonstrated that large skyrmion deformation can reduce the total free energy. To further investigate the elastic properties of the skyrmion lattices, both lattice strain and particle strain are determined [39]. As presented in Fig. 11(a), lattice strain concentrates at the grain boundary regions, particularly around the sevenfold skyrmion. Moving away from the grain boundary, the magnitude of lattice strain decreases gradually and approaches zero in the perfect lattice region far from the grain boundary. This indicates that the lattice mismatch caused by the presence of the grain boundary is relaxed by thorough positional adjustments of individual skyrmions. Such a relaxation mechanism is analogous to that in conventional atomic grain boundaries.

Under the low magnetic field condition ($H = 1.0 \times 10^5$ A/m), the lattice strain distribution changes significantly. As shown in Fig. 11(b), the tensile lattice strain in the grain boundary region intensifies, especially around the sevenfold skyrmion. Simultaneously, the compressive lattice strain near the fivefold skyrmion decreases. The high lattice strain consequently exhibits substantial deformation in the sevenfold skyrmion. In addition, the skyrmions have not moved significantly. As shown in Fig. 11(b), the tensile lattice strain in the grain boundary region intensifies strongly. In contrast to the reference condition, no appreciable lattice strain is distributed in other regions. At the same time, skyrmion deformations at the grain boundary become more pronounced. This indicates that, under low magnetic field conditions, the relaxation mechanism totally changes. In other words, lattice mismatch is maintained by local skyrmion deformations rather than relaxed by positional shifts of skyrmions. This is a quasiparticle-based stabilization mechanism unique to skyrmions, which is fundamentally different from conventional lattice behavior.

VI. CONCLUSION

This work presented a comprehensive phase-field simulation of the temperature and magnetic field dependence of grain boundary structures in MnSi thin films. Skyrmion grain boundaries are formed by arrays of dislocation cores, similar to those in atomic crystals, but their stabilization relies on the skyrmion deformations, particularly the fivefold and sevenfold skyrmions. Skyrmion morphology strongly depends on external conditions: deformation near the grain boundary is significantly enhanced at lower temperature and lower magnetic fields. The underlying mechanism for this deformation is identified as a competition between fundamental magnetic interactions. Specifically, the local skyrmion deformation is driven by the decrease of DM interaction energy, which makes the deformed state energetically favorable in the vicinity of the grain boundary. Furthermore, the local skyrmion deformation accommodates the lattice mismatch at the grain boundary, in contrast to conventional relaxation by positional shifts. This quasiparticle-based relaxation highlights a fundamental distinction between skyrmion lattices and conventional crystalline materials. These findings not only advance the fundamental understanding of defect structures in topological magnetic systems but also hold significant value for the development of advanced spintronic devices.

ACKNOWLEDGMENTS

This work is supported by Japan Society for the Promotion of Science (JSPS) KAKENHI (Grants No. JP23H00159, No. JP23K17720, No. JP24H00032, No. 25K22058, and No. 25KF0044), Japan Science and Technology Agency FOREST Program (Grant No. JPMJFR222H), JSPS SPRING (Grant No. JPMJSP2110), JSPS Postdoctoral Fellowship (Grant No. P24352), the National Natural Science Foundation of China (Grant No. 12402194), and the Hunan Provincial Natural Science Foundation of China (Grant No. 2025JJ60053).

DATA AVAILABILITY

The data that supports the findings of this article cannot be made publicly available because no suitable repository exists for hosting data in this field of study. The data are available upon reasonable request from the authors.

[1] S. Muülbauer, B. Binz, F. Jonietz, C. Pfleiderer, A. Rosch, A. Neubauer, R. Georgii, and P. Böni, Science **323**, 915 (2009).
[2] N. Kanazawa, S. Seki, and Y. Tokura, Adv. Mater. **29**, 1603227 (2017).
[3] A. Neubauer, C. Pfleiderer, B. Binz, A. Rosch, R. Ritz, P. G. Niklowitz, and P. Böni, Phys. Rev. Lett. **102**, 186602 (2009).
[4] N. Nagaosa and Y. Tokura, Nat. Nanotechnol. **8**, 899 (2013).
[5] R. Tomasello, E. Martinez, R. Zivieri, L. Torres, M. Carpentieri, and G. Finocchio, Sci. Rep. **4**, 6784 (2014).
[6] X. Zhang, M. Ezawa, and Y. Zhou, Sci. Rep. **5**, 9400 (2015).
[7] K. M. Song, J.-S. Jeong, B. Pan, X. Zhang, J. Xia, S. Cha, T.-E. Park, K. Kim, S. Finizio, J. Raabe, J. Chang, Y. Zhou, W. Zhao, W. Kang, H. Ju, and S. Woo, Nat. Electron. **3**, 148 (2020).
[8] X. Z. Yu, Y. Onose, N. Kanazawa, J. H. Park, J. H. Han, Y. Matsui, N. Nagaosa, and Y. Tokura, Nature (London) **465**, 901 (2010).
[9] P. Huang, T. Schönenberger, M. Cantoni, L. Heinen, A. Magrez, A. Rosch, F. Carbone, and H. M. Rønnow, Nat. Nanotechnol. **15**, 761 (2020).
[10] P. Baláž, M. Paściak, and J. Hlinka, Phys. Rev. B **103**, 174411 (2021).
[11] K. Karube, J. S. White, N. Reynolds, J. L. Gavilano, H. Oike, A. Kikkawa, F. Kagawa, Y. Tokunaga, H. M. Rønnow, Y. Tokura, and Y. Taguchi, Nat. Mater. **15**, 1237 (2016).
[12] K. Shibata, J. Iwasaki, N. Kanazawa, S. Aizawa, T. Tanigaki, M. Shirai, T. Nakajima, M. Kubota, M. Kawasaki, H. S. Park, D. Shindo, N. Nagaosa, and Y. Tokura, Nat. Nanotechnol. **10**, 589 (2015).
[13] X. Yu, D. Morikawa, T. Yokouchi, K. Shibata, N. Kanazawa, F. Kagawa, T.-h. Arima, and Y. Tokura, Nat. Phys. **14**, 832 (2018).
[14] M. Nagao, Y.-G. So, H. Yoshida, T. Nagai, K. Edagawa, K. Saito, T. Hara, A. Yamazaki, and K. Kimoto, Appl. Phys. Express **8**, 033001 (2015).
[15] Z.-A. Li, F. Zheng, A. H. Tavabi, J. Caron, C. Jin, H. Du, A. Kovács, M. Tian, M. Farle, and R. E. Dunin-Borkowski, Nano Lett. **17**, 1395 (2017).
[16] J. Rajeswari, P. Huang, G. F. Mancini, Y. Murooka, T. Latychevskaia, D. McGrouther, M. Cantoni, E. Baldini, J. S. White, A. Magrez, T. Giamarchi, H. M. Rønnow, and F. Carbone, Proc. Natl. Acad. Sci. USA **112**, 14212 (2015).
[17] H. Nakajima, A. Kotani, M. Mochizuki, K. Harada, and S. Mori, Appl. Phys. Lett. **111**, 192401 (2017).
[18] S. Pöllath, J. Wild, L. Heinen, T. N. G. Meier, M. Kronseder, L. Tutsch, A. Bauer, H. Berger, C. Pfleiderer, J. Zweck, A. Rosch, and C. H. Back, Phys. Rev. Lett. **118**, 207205 (2017).
[19] T. Matsumoto, Y.-G. So, Y. Kohno, H. Sawada, Y. Ikuhara, and N. Shibata, Sci. Adv. **2**, e1501280 (2016).
[20] T. Schönenberger, P. Huang, L. D. Brun, L. Guanghao, A. Magrez, F. Carbone, and H. M. Rønnow, Nanoscale Res. Lett. **17**, 20 (2022).
[21] T. Shimada, Y. Uratani, and T. Kitamura, Appl. Phys. Lett. **100**, 162901 (2012).
[22] H. Gleiter, Acta Metall. **27**, 187 (1979).
[23] M. Upmanyu, D. Srolovitz, L. Shvindlerman, and G. Gottstein, Interface Sci. **6**, 289 (1998).
[24] Z. Gong, W. Zhao, K. Guan, P. Rao, Q. Zeng, J. Liu, and Z. Feng, J. Am. Ceram. Soc. **103**, 5900 (2020).
[25] M. D. Sangid, H. J. Maier, and H. Sehitoglu, Int. J. Plast. **27**, 801 (2011).
[26] T. Uesugi and K. Higashi, Mater. Trans. **54**, 1597 (2013).
[27] Y. Wang, R. Manabe, K. Kasai, T. Xu, and T. Shimada, Acta Mater. **281**, 120381 (2024).
[28] U. K. Rößler, A. N. Bogdanov, and C. Pfleiderer, Nature (London) **442**, 797 (2006).
[29] Y. Ni, L. He, and A. G. Khachaturyan, J. Appl. Phys. **108**, 023504 (2010).

[30] A. Gordon, I. D. Vagner, and P. Wyder, Phys. Rev. B **41**, 658 (1990).
[31] X. Lu, H. Li, and B. Wang, J. Mech. Phys. Solids **59**, 1966 (2011).
[32] L. Q. Chen and J. Shen, Comput. Phys. Commun. **108**, 147 (1998).
[33] Y. Wang, J. Wang, T. Kitamura, H. Hirakata, and T. Shimada, Phys. Rev. B **106**, 094423 (2022).
[34] T. Shimada, Y. Umeno, and T. Kitamura, Phys. Rev. B **77**, 094105 (2008).
[35] Y. C. Wang and H. Q. Ye, Philos. Mag. A **75**, 261 (1997).
[36] S. Zhang, Z. Xie, P. Keuter, S. Saood, L. Abdellaoui, X. Zhou, N. Cautaerts, B. Breitbach, S. Aliramaji, S. Korte-Kerzel, M. Hans, J. M. Schneider, and C. Scheu, Nanoscale **14**, 18192 (2022).
[37] K.-J. Bathe, E. Ramm, and E. L. Wilson, Int. J. Numer. Methods Eng. **9**, 353 (1975).
[38] A. Stukowski, JOM **66**, 399 (2014).
[39] K. Kasai, T. Xu, S. Minami, and T. Shimada, Nano Lett. **24**, 13247 (2024).